Journal of Magnetic Resonance 281 (2017) 199–208

Contents lists available at ScienceDirect

Journal of Magnetic Resonance

journal homepage: www.elsevier.com/locate/jmr

Quadrupolar nutation NMR to discriminate central and satellite transitions: Spectral assignments for a Ziegler-Natta catalyst

E.S. (Merijn) Blaakmeer [a,b], Wouter M.J. Franssen [a], Arno P.M. Kentgens [a,*]

[a] Radboud University, Institute for Molecules and Materials, Heyendaalseweg 135, 6525 AJ Nijmegen, The Netherlands
[b] Dutch Polymer Institute (DPI), P.O. Box 902, 5600 AX Eindhoven, The Netherlands

ARTICLE INFO

Article history:
Received 20 April 2017
Revised 21 May 2017
Accepted 3 June 2017
Available online 7 June 2017

Keywords:
Nutation NMR
Central transition
Satellite transition
Half-integer quadrupole nuclei
$MgCl_2$
Ziegler-Natta catalysts

ABSTRACT

In this contribution we used solid state ^{35}Cl ($I = 3/2$) quadrupolar NMR to study a $MgCl_2$/2,2-dimethyl-1,3-dimethoxypropane (DMDOMe) adduct that serves as a model system for Ziegler-Natta catalysis. Employing large Radio-Frequency (RF) field strengths we observe three spectral features with strongly varying line widths. The assignment of the spectra is complicated because of the large difference in quadrupolar interactions experienced by the different sites in the system. The satellite transitions (ST) of relatively well-defined bulk Cl sites are partially excited and may overlap with the central transition (CT) resonances of more distorted surface sites. We show that nutation NMR of the ST of $I = 3/2$ spins yields a unique pattern that makes a clear distinction between an extensively broadened central transition and the satellite transitions of a component with a smaller quadrupolar interaction. This allows us to unambiguously unravel the spectra of the $MgCl_2$ adduct showing that we observe CT and ST of the bulk phase of $MgCl_2$-nanoparticles with a C_Q of 4.6 MHz together with the CT of surface sites displaying an average C_Q of ~10 MHz.

1. Introduction

Solid state nuclear magnetic resonance (NMR) spectroscopy is extensively used in materials science owing to the sensitivity of the nuclear spin to the local environment. In this paper we focus on the $MgCl_2$-support in a binary adduct between $MgCl_2$ nanoparticles and an organic electron donor (2,2-dimethyl-1,3-dimethoxy propane/DMDOMe), see Figs. SI 1 and SI 2. This adduct serves as a model system for Ziegler-Natta catalysis [1,2] and is studied using ^{35}Cl solid state NMR.

The structure of α-$MgCl_2$ consists of Cl-Mg-Cl triple layers in which each Mg is octahedrally coordinated by the chlorine [3]. This results in a moderate quadrupolar parameter for the ^{35}Cl nucleus: $C_Q = 4.6$ MHz [4]. The $MgCl_2$ nanoparticles in our adduct still have a relatively well-defined bulk phase, with some distribution in the quadrupolar parameters resulting from the heterogeneity of the sample. Besides this, they also have large surface areas that expose unsaturated sites which are important for catalysis. The focus in the literature is in particular on the (1 0 4)- and (1 1 0)-surface sites [5–7] as well as surface defects [1,8] which, due to their asymmetric environment, are both expected to exhibit large quadrupolar couplings. In a previous publication, we calculated that the quadrupolar parameters for the (1 0 4)- and (1 1 0)-surface sites are 10–16 MHz [9], yielding line widths (~250–700 kHz) that cannot be averaged by current MAS technology thus implying that they should be detected and characterized by static ^{35}Cl experiments. In our current binary system at least part of these surface sites will be coordinated by the organic donor. The NMR parameters of such donor-bound surface sites are not reported, although preliminary calculations suggest that they are comparable to the naked surfaces. It is of great interest to learn more about the exact coordination of the donor on the support, and the detection of relevant surface sites is key to this.

In the case of nuclei with $I > 1/2$ (such as ^{35}Cl, so-called quadrupolar nuclei) the resulting NMR spectrum can be complex due to the overlap of multiple, broad powder patterns. When spectra lack clear features, as is the case for disordered or heterogeneous samples like our catalyst, the interpretation of the spectrum becomes even more troublesome. Magic angle spinning (MAS) already significantly narrows the quadrupolar broadened lines by a factor of ~3 [10,11]. Yet, the second-order broadened line shapes may still overlap and analysing the 1D spectrum can be complicated. The MQMAS pulse sequence [12,13] has been successfully introduced as a method to resolve overlapping sites in a

* Corresponding author.
E-mail addresses: m.blaakmeer@science.ru.nl (E.S. (Merijn) Blaakmeer), w.franssen@science.ru.nl (W.M.J. Franssen), a.kentgens@nmr.ru.nl (A.P.M. Kentgens).

http://dx.doi.org/10.1016/j.jmr.2017.06.002
1090-7807/

2D fashion. Alternatively, nutation NMR under static conditions [14,15] can be used to differentiate between overlapping sites and extract the relevant NMR (quadrupolar) parameters.

The heydays of nutation NMR were the 80's and 90's, before the introduction of the MQMAS sequence. However, recently our group [16] showed that nutation NMR, owing to the high RF field strengths available when using milli- and microcoils, can be a valuable tool for systems where the quadrupolar interaction becomes too large to be averaged by means of MAS. At an RF field strength of 100 kHz spin systems with quadrupolar frequencies, $\omega_Q = 3C_Q/(2I(2I-1))$, of up to 1 MHz can be studied. This is extended to 10 MHz when the RF is increased to 1 MHz, which means that, for $I = 3/2$, spin systems with quadrupolar coupling constants, $C_Q = e^2qQ/h$, of up to 20 MHz become accessible [15]. For larger spin quantum numbers even much larger C_Q's can be handled. Such systems would require spinning speeds of many hundreds of kilohertz, that cannot be achieved by current MAS technology.

Very broad resonances can still be observed using static approaches and over the years multiple techniques have been developed for the characterization of wideline spectra [17]. Frequency-swept pulses of the WURST-class [18,19] are used for broadband excitation. They are combined with QCPMG detection [20–22] for enhanced sensitivity and are sometimes combined with frequency stepped acquisition [23] for ultra-wideline spectra. These approaches work well and even the presence of multiple non-equivalent sites has been shown [24–26]. However, despite the large quadrupolar parameters and hence asymmetric environments, they are still well-defined crystallographic sites.

A problem arises in the characterization of systems containing sites with a certain degree of disorder combined with large differences in their respective quadrupolar parameters. In such cases line shapes lack distinct spectral features and satellite transitions (ST) of relatively symmetric sites and central transitions (CT's) of distorted sites will overlap. Hence the identification of ST line shapes versus CT line shapes becomes obscured. An example includes the ^{75}As spectra of $Al_xGa_{1-x}As$ semiconductors, which give rise to two narrow lines from locally symmetric As[Al_4] and As[Ga_4] sites that can be straightforwardly observed [27]. CT signals from the other As[Al_nGa_4-n] ($n = 1, 2, 3$) sites span >1 MHz and could only be characterized using high RF fields [28], but there is strong overlap between the satellite transitions (ST) and central transitions (CT's). In this example distinct quadrupolar features and DFT modelling aids in the final assignment of the spectra. Another example of ST/CT overlap is the ^{91}Zr study of a zirconocene where dominant signals from chlorine ST almost obscure the ^{91}Zr CT signal [25]. In general, it can become very difficult to infer to what extent broad resonances are the results of ST from sites with low C_Q or CT's from sites with much higher C_Q, or even a combination of both. This is especially the case for disordered or heterogeneous samples which lack clear quadrupolar features in their line shapes. In this contribution we show how nutation NMR can be exploited to differentiate between a satellite transition and an extensively broadened central transition and in this way we can unambiguously interpret the ^{35}Cl spectrum of our $MgCl_2$-nanoparticles.

2. Theory

A nutation experiment follows the modulation of the observed NMR signal as a function of the duration of the excitation pulse (t_1 dimension). The presence of a strong quadrupolar interaction cannot be neglected during the pulse duration and the effective Hamiltonian during the pulse has therefore contributions from both RF and quadrupolar parts. This leads to mixing of the Zeeman states during the evolution period t_1 such that the CT coherences is modulated by $2I$ frequencies during the pulse, in the case of on-resonance irradiation. The resulting nutation profile can be used to deduce the quadrupolar parameters of the systems under study and resolve the presence of overlapping sites in the 1D spectrum [29–31].

At various relative strengths of ν_Q and ν_{RF} the observed nutation behaviour of the CT of a quadrupolar nucleus can deviate strongly from the expected RF field strength, see Fig. SI 3. When the RF field strength is much stronger than the quadrupolar frequency ($\nu_Q \ll \nu_{RF}$), predominantly the "regular" ($I = 1/2$) nutation frequency at ν_{RF} is observed. In the opposite case, when the quadrupolar coupling is large compared to the RF field strength ($\nu_{RF} \ll \nu_Q$), a single nutation frequency is observed at $(I + 1/2) \times \nu_{RF}$. However, in the so-called intermediate nutation regime ($0.1 \leqslant \nu_Q/\nu_{RF} \leqslant 10$) a characteristic profile of nutation frequencies is obtained [14,15,32], see Fig. SI 3.

During rf-irradiation the spin states, labelled 1–4 for a spin $I = 3/2$, are mixtures of the $|I, m\rangle$ functions. Their energy levels are shown in Fig. 1A as a function of Ω_Q/ν_{RF}, with the angular dependent quadrupolar frequency $\Omega_Q = \omega_Q/2((3\cos^2\theta - 1) + \eta_Q \cos 2\phi \sin^2\theta)$. In the absence of a quadrupolar interaction ($\Omega_Q/\nu_{RF} \approx 0$) four equally spaced energy levels are found with an energy difference of ν_{RF}. The associated transition frequencies for the most prominent transitions are shown in Fig. 1B and they show a strong dependence on Ω_Q/ν_{RF}. The evolution of these transitions contribute differently to the transitions between the $|I, m\rangle$ spin levels observed directly after the nutation pulse. Evolution of the density matrix allows the computation of the amplitude factors $(R_{i,j})_{m,n}$ describing the contribution of a transition $i \Longleftrightarrow j$ during rf-irradiation to an observed transition $m \Longleftrightarrow n$ during detection [32]. Fig. 1C displays the amplitudes of the various transitions in the nutation frame contributing to the observed CT intensities (for spin $I = 3/2$) at the end of the pulse. This shows that at high Ω_Q/ν_{RF} ratio, the dominant nutation frequency is $2 \times \nu_{RF}$. The ST are modulated by the same $2I$ nutation frequencies. The corresponding amplitudes contributing to the observed ST intensities are shown in Fig. 1D. The $2 \Longleftrightarrow 3$ transition has the highest amplitude, but the amplitudes of the three frequencies are of similar size and all become smaller at larger Ω_Q/ν_{RF}. In contrast to the CT, there is not a dominant nutation frequency at higher Ω_Q/ν_{RF}-ratio's.

Fig. 2B shows a simulated ^{23}Na ($I = 3/2$) full 2D nutation spectra with contributions from both CT and ST. This spectrum is simulated for a model system: Na_2SO_4, which is characterized by $C_Q = 2.60$ MHz and $\eta = 0.58$ [33] using $\nu_{RF} = 133$ kHz at a magnetic field of 9.4 T. The projected trace in F2 shows the regular 1D spectrum where some features of the satellites can just be identified. The projected trace in F1 is generally referred to as the nutation spectrum that can also be obtained by an alternative pseudo 2D processing: direct Fourier transformation of the FID maximum. The advantage of a full 2D spectrum is that the nutation frequencies of every point in the regular 1D spectrum can be retrieved, although it requires a high S/N-ratio to see the satellites.

Fig. 2 shows that the satellite transition nutation frequencies display a characteristic pattern. The on-resonance ST powder pattern is always symmetric, because both satellite transitions are observed simultaneously. The nutation spectrum is therefore, in principle, symmetric around the isotropic shift of the ST. The pattern that is observed corresponds to the calculated transitions frequencies in 1B. Any particular position in the satellite manifold, at a frequency $\pm\nu$ relative to the isotropic shift, has a certain angular dependent quadrupolar frequency, Ω_Q and it will thus give the three nutation frequencies corresponding to the ratio Ω_Q/ν_{RF}. This creates a unique butterfly-like pattern which can be clearly set apart from the much broader and distributed nutation profile of any CT that may resonate at the same position.

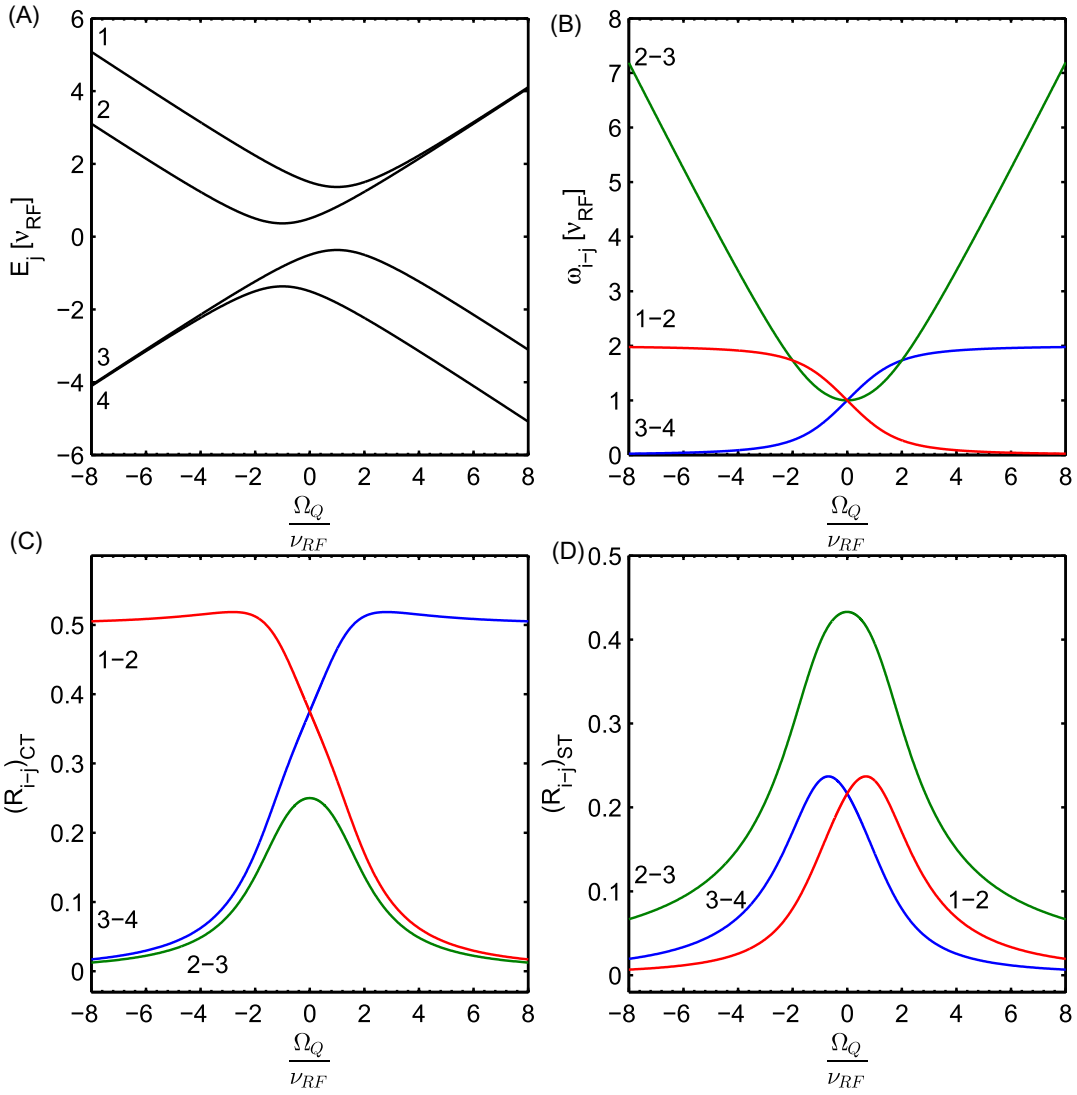

Fig. 1. Simulations for a spin $I = 3/2$ showing (A) energy levels in the rotating frame during rf-irradiation (E_j), (B) associated transition frequencies (ω_{i-j}), (C) amplitudes factors describing the contributions of the $i \Longleftrightarrow j$ transitions to the central transition $(R_{i-j})_{CT}$ and (D) and the satellite transitions $(R_{i-j})_{ST}$ in the observed spectrum.

Fig. 2A shows the experimental ^{23}Na 2D nutation spectrum for Na_2SO_4, obtained at ν_{RF} = 133 kHz and whole echo detection. With these settings ($\nu_{RF} \leqslant \nu_Q$) the CT predominantly shows a nutation frequency of $2 \times \nu_{RF}$ as is indeed observed in both the simulation and the experiment. In the experiment there is an asymmetric broadening that results from RF inhomogeneities, see Fig. SI 4. Irrespective of the relative low ν_{RF}/ν_Q ratio, the satellite transitions show the characteristic pattern of three frequency ridges. This perfect match between simulation and experiment shows the potential of nutation NMR for discriminating satellite transitions from central transitions.

The position-dependency of the nutation frequencies means that, independent of C_Q, the satellite nutation pattern will in principle always have the same shape and just stretches out further along the F2 dimension for systems with higher C_Q. This is shown in Fig. 2D, which is simulated using the same ν_{RF} as Fig. 2B, but for a system with larger quadrupolar parameters: C_Q = 5.0 MHz and η = 0.2. With this larger quadrupolar coupling it becomes apparent that the nutation pattern of the ST and the CT are slightly shifted with respect to each other in the F2 dimension, as the result of the different quadrupole induced shifts of the transitions [34]. The shape of the satellite nutation pattern is also independent of ν_{RF}. Varying ν_{RF} leads to a scaling along both the F1 and F2 dimension, see Fig. 2C. It can be understood by looking at Fig. 1B in which both axes are expressed in units of ν_{RF}. Indeed, at higher ν_{RF} the same Ω_Q/ν_{RF} ratio is only reached at higher Ω_Q and the nutation pattern will thus be stretched along F2, provided that the required Ω_Q still falls within the satellite manifold. The intersections of the nutation frequencies will always occur at ν_{RF} for $\Omega_Q/\nu_{RF} = 0$ and just below $2 \times \nu_{RF}$ for $\Omega_Q/\nu_{RF} = 2$. The nutation pattern will therefore also be stretched along F1 for a higher ν_{RF}, as can be seen indeed in Fig. 2C in which ν_{RF} is increased to 200 kHz.

At fixed ν_{RF} the nutation frequency found for a crystallite with a certain angular dependent quadrupolar frequency, Ω_Q, will always be the same and therefore the nutation pattern is virtually independent of η as well. Fig. 2D is simulated using an η = 0.2 and indeed the same shape is obtained. The powder spectra of the satellite transitions are in first order symmetric around the centre frequency with their intensity distribution governed by η and therefore η only affects the intensities of the observed nutation frequency ridges but not their overall profile. As a result, the choice of η for the simulation is actually not very important, neither does it

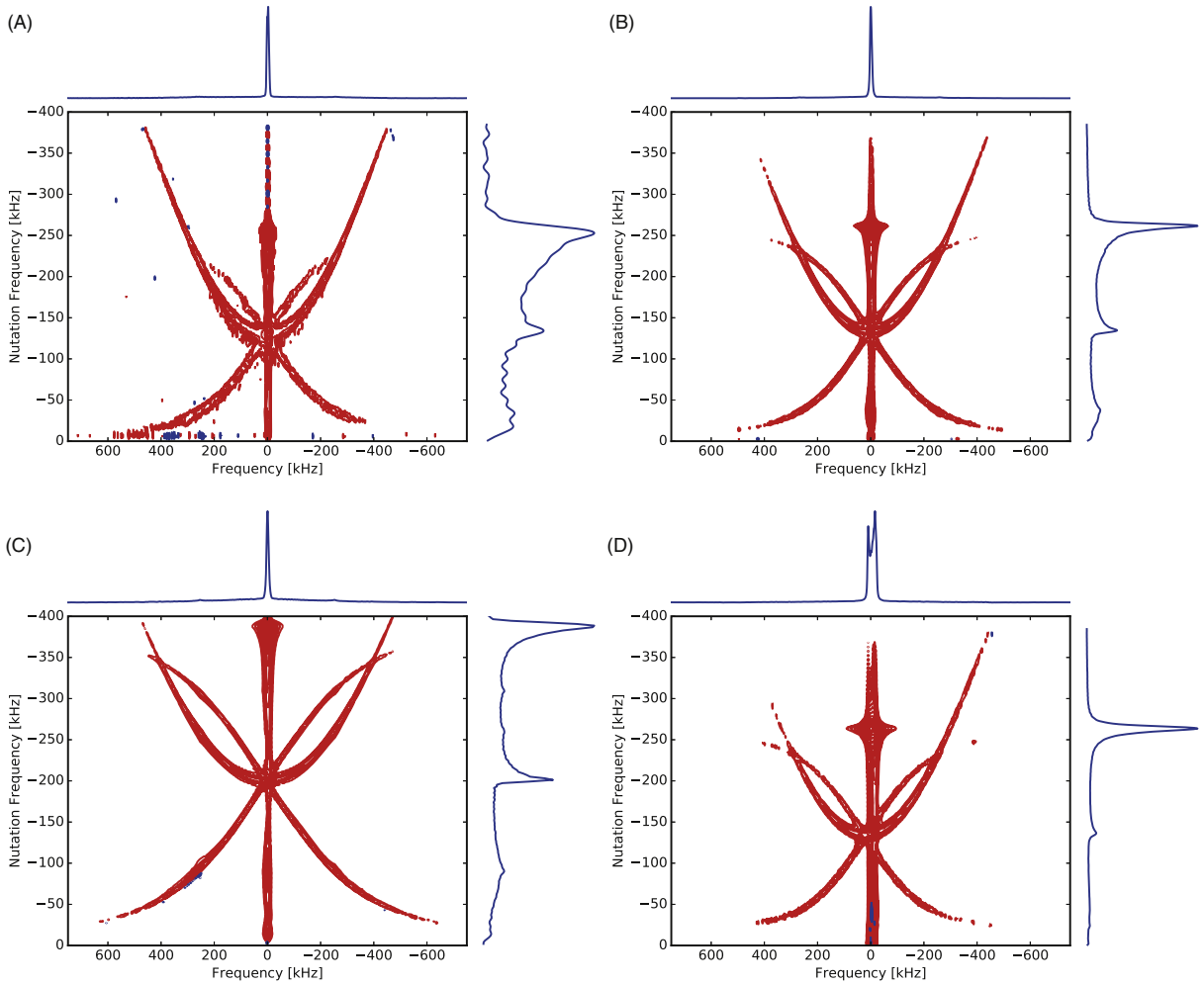

Fig. 2. (A) Experimental static on-resonance ^{23}Na full 2D nutation spectrum of Na_2SO_4 detected via solid echo with whole echo detection using ν_{RF} = 133 kHz at 9.4 T. Simulated full 2D whole echo detected nutation spectra for Na_2SO_4 using (B) ν_{RF} = 133 kHz, (C) ν_{RF} = 200 kHz and (D) ν_{RF} = 133 kHz, but for a system with C_Q = 5.0 MHz and η = 0.2. Negative and positive amplitudes are shown by blue and red contour levels, respectively. (For interpretation of the references to colour in this figure legend, the reader is referred to the web version of this article.)

matter if the system under study has well-defined or distributed quadrupolar parameters.

3. Results & discussion

3.1. Hahn echo

All ^{35}Cl experiments were performed using a home-built probe with an inner-coil diameter of 1.2 mm which reached an RF field strength (ν_{RF}) of 480 kHz at a power of 1120 W and a frequency ν_L of 78.3 MHz. Fig. 3 shows the ^{35}Cl Hahn echo spectrum of the $MgCl_2$/DMDOMe adduct (bottom trace) at this high RF field strength. Crystalline $MgCl_2$ is characterized by a ^{35}Cl C_Q of 4.6 MHz, with η = 0 [4]. In the case of nanoparticles, as studied here, the resulting ^{35}Cl spectrum will be a somewhat less well-defined, because of the heterogeneity in the sample giving a distribution of quadrupolar parameters [4,9]. Still, this gives a 'narrow' CT line, which is ±50 kHz broad at a static magnetic field of 18.8 T. This corresponds to spectral component **A** (CT_A) in Fig. 3. Since ^{35}Cl has a spin quantum number of I = 3/2, the corresponding satellite transitions of the bulk (ST_A) will span a frequency range of approximately −2.3 to +2.3 MHz. Due to its width and the limited bandwidth of the probe the full satellite pattern is not readily observed in a single experiment. Consequently, the spectrum obtained near the resonance frequency of CT_A, will only show part of the signal from ST_A which will overlap with potential signal from the surface sites.

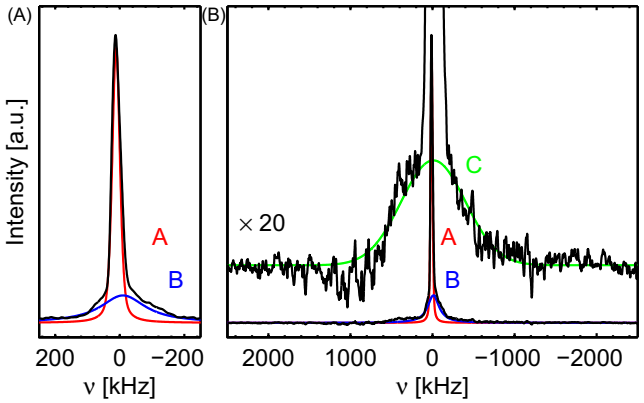

Fig. 3. On-resonance ^{35}Cl Hahn echo spectrum of the $MgCl_2$ adduct at ν_{RF} = 480 kHz; with (A) showing an enlargement of the narrow signals and *B* showing the full spectrum. The spectrum is divided into three different components, which are for illustrative purposes approached by Gaussian functions. They are labelled **A**, **B** and **C** and are coloured red, blue and green respectively. (For interpretation of the references to colour in this figure legend, the reader is referred to the web version of this article.)

Besides the 'narrow' CT_A, the bottom trace in Fig. 3 shows a second broader component spanning ~350 kHz. This spectral component **B** also lacks well-defined features. Owing to our high RF field strength we can be sure of a proper excitation of this component. It is also observed with somewhat lower RF field strengths and field dependent measurements show an inverse scaling with the magnetic field. The signal can therefore be assigned to a CT of a site with a moderate quadrupolar coupling ($C_Q \sim 10$ MHz). This assignment is further corroborated by the nutation experiments (vide infra). Spectral component **B** can be identified as a surface site of the $MgCl_2$ nanoparticles. A further detailed description of this surface site is beyond the scope of this article and will be addressed in a forthcoming publication studying different adducts.

A vertical expansion (the top trace) shows yet another, much broader component spanning almost 2 MHz, spectral component **C**. Owing to the high RF field, we are able to excite such a broad resonance. The interpretation of this spectral feature is bound to be troublesome. Spectral component **C** is rather symmetric without specific features. Its width might be limited by the probe's bandwidth. Due to its rather featureless appearance and the uncertainty in its exact span, it is unsure how this signal should be interpreted: is it a second surface site, or is it part of ST_A or an overlap of both? It should be noted that the broad component has a significant intensity (±1/3 estimated from the FID), although experimental conditions do not permit an exact quantitative interpretation.

3.2. Variable offset cumulative spectra

To obtain the full spectrum the best approach would be to take spectra at variable offsets, using broadband excitation techniques to minimize the number of frequency steps that needs to be taken. We performed variable offset cumulative spectra (VOCS) over a frequency range from 74.1 to 81.1 MHz using high power excitation ($\nu_{RF} \sim$ of 480 kHz), see Fig. 4 and Fig. SI 5. Due to the low vertical intensity of the satellite signal, many scans were needed to get a decent quality for each individual echo. All echoes were acquired with recycle delays of 200 ms with up to 400,000 scans each, giving an experimental time per echo of almost 22 h. The complete VOCS therefore took more than a full week to record.

Fig. 4 shows signal spanning from −5 to +3 MHz. At ~74.4 MHz we reach the Larmor frequency of ^{91}Zr and observe the signal from the ZrO_2 rotor [35]. The satellite transitions of this Zr site also explain the features at 74.8 and 75.5 MHz. The resulting ^{35}Cl signal seems to extend a bit beyond the theoretical value of ±2.3 MHz, but this may well be related to the distribution in quadrupolar parameters of $MgCl_2$. The observed signal lacks well-defined features. It is most intense near the central transition and decreases in intensity at larger offsets, again in agreement with the distribution in quadrupolar parameters. Fig. 4 includes a simulation of the full spectrum (CT + ST) of a system with $C_Q = 4.6$ MHz and $\eta = 0.6$. A decent agreement between the simulation and experiment is achieved, suggesting that spectral component **A** and **C** could be assigned as CT_A and ST_A.

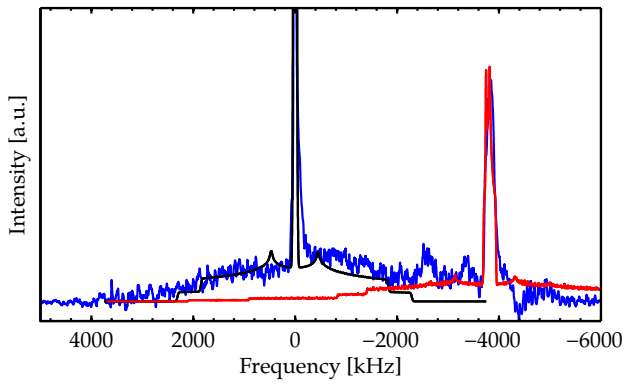

Fig. 4. Static ^{35}Cl spectrum of the $MgCl_2$ adduct acquired using VOCS. The overall spectrum (blue) is the result of summing 11 Hahn echoes (see Fig. SI 5) with rf carrier frequency step size of 700 kHz. Spectra were collected at 18 T using $\nu_{RF} \sim$ of 480 kHz. Black: simulation of a ^{35}Cl crystalline phase with $C_Q = 4.6$ MHz and $\eta = 0.6$. Red: simulation of ^{91}Zr signal from the rotor ($C_Q = 19.6$ MHz, $\eta = 0.6$ [35]). (For interpretation of the references to colour in this figure legend, the reader is referred to the web version of this article.)

However, agreement between simulation and experiment is not perfect and it cannot be excluded that there is still overlap between ST_A and potential surface sites. To this end we would need field dependant VOCS measurements, but this is a time consuming process and therefore not the most optimal experiment. We resort to nutation NMR to study spectral component **C** in more detail.

3.3. On-resonance nutation

For the bulk phase of α-$MgCl_2$ ($\nu_Q = 2.3$ MHz) a 480 kHz strong RF field fulfils the condition for the intermediate nutation regime ($0.1 \leqslant \nu_Q/\nu_{RF} \leqslant 10$). The CT of the bulk phase is thus expected to show multiple nutation frequencies. Any additional CT's with much larger quadrupolar couplings should only give one nutation frequency at $2 \times \nu_{RF}$. The nutation frequency of satellite transitions in turn will show the characteristic three nutation frequency ridges as was discussed in the theory section.

The experimental on-resonance ^{35}Cl nutation spectrum for the $MgCl_2$ adduct is shown in Fig. 5 along with some simulated nutation spectra. These nutation spectra are obtained by Fourier transformation of the FID maxima. This processing procedure is chosen because the intensity of spectral component ST_A contributes significantly to the intensity in the FID while it hardly stands out of the noise in the spectra due to its width. The resulting experimental nutation profile will thus include the contribution from all the potential CT's and ST present in the spectrum. An exception to this procedure is the bottom spectrum in Fig. 5B, which shows a slice from the full 2D experimental nutation spectrum at the position of the transmitter offset. Consequently this will almost exclusively give signal from CT_A.

Simulated nutation spectra are performed for a ^{35}Cl nucleus with $C_Q = 4.6$ MHz or $C_Q = 10$ MHz and $\eta = 0.6$ at an external magnetic field strength of 18.8 T ($\nu_L = 78.3$ MHz) and an applied ν_{RF} of 480 kHz, to model the nutation behaviour of spectral components **A** and **B**. The detection bandwidth of the probe is not included in the simulations, which therefore includes the full contributions from the whole satellite pattern. As a result the simulations will overrepresent the ST contribution with respect to the experiment, as here the satellites' contribution is limited due to the probes bandwidth. To investigate the individual contributions of the ST and CT to the total nutation spectrum, separated nutation spectra are also simulated for the ST and CT of spectral component **A**, see Fig. 5B.

The simulated spectrum of bulk $MgCl_2$ ($CT_A + ST_A$, Fig. 5A) shows a broad range of frequencies with dominant peaks around 900 and 490 kHz. The nutation spectrum of only the satellites show that the nutation frequency at 490 kHz originates mainly from the satellite transitions of bulk $MgCl_2$ (Fig. 5B). CT_A gives a weak peak at 490 kHz and a stronger signal around 900 kHz. This frequency of 900 kHz is somewhat below $2 \times \nu_{RF}$. Spectral component **B** has a much larger C_Q than bulk $MgCl_2$ and ν_Q/ν_{RF} reaches the limit of the intermediate nutation regime, therefore CT_B will nutate at $\approx 2 \times \nu_{RF}$. This is indeed what is simulated in the top trace of Fig. 5A. Its corresponding ST span 10 MHz which, in combination with its lower intensity, mean that it will not be detected

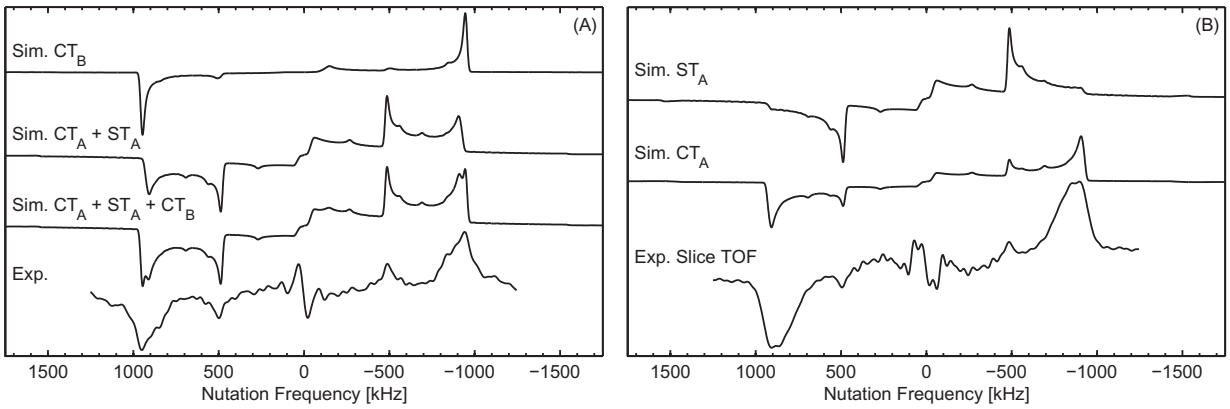

Fig. 5. Simulated and experimental ^{35}Cl nutation spectrum for the $MgCl_2$ adduct at ν_{RF} = 480 kHz at a frequency of 78.3 MHz (on-resonance). All spectra are processed by Fourier transformation of the echo maxima, except for the bottom trace in (B) which is taken as slice from the full 2D nutation spectrum at the position of the transmitter offset. The experiment was measured accumulating 18,432 scans per echo, 60 increments, and took a 62 h to complete.

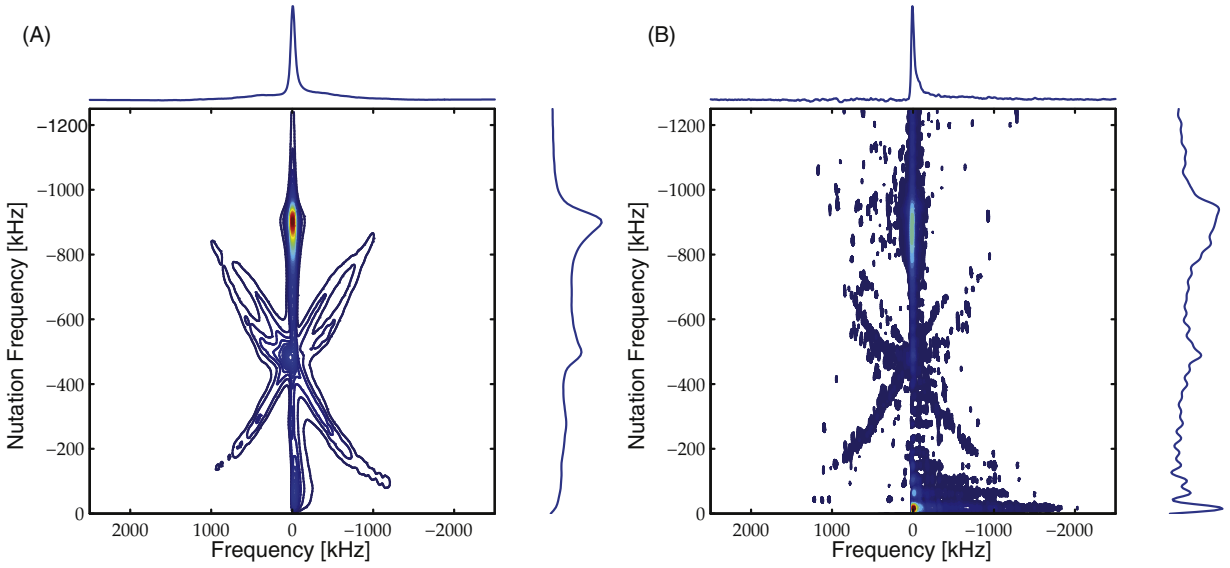

Fig. 6. (A) Simulated and (B) experimental on-resonance full 2D nutation spectra detected via an echo pulse for the $MgCl_2$ adduct at an external magnetic field strength of 18.8 T and a ν_{RF} of 480 kHz.

above the noise. The contributions from ST_B is therefore not included in our analysis.

The experimental nutation spectrum (Fig. 5A) shows two frequencies: a dominant broad band at 950 kHz and a weaker peak at 490 kHz. The slice taken at the position of the transmitter offset shows a slightly different nutation spectrum (Fig. 5B). It is dominated by an intense peak at 900 kHz and the peak at 490 kHz is even weaker. This matches quite well with the simulated nutation spectrum of CT_A. Processing the experimental spectrum via Fourier transformation of the echo maximum should give a higher contribution from ST in the nutation spectrum and indeed the 490 kHz peak is more intense. However, since the ST are only partly excited in the experimental spectrum their contribution is strongly reduced in the nutation profile compared to the simulated spectrum for $CT_A + ST_A$. The shift of the peak maxima from 900 to 950 kHz can be explained by a contribution of nutation frequencies from CT_B as can be seen in weighted sum of the nutation spectra of components **A** and **B** in Fig. 5A.

The experimental nutation profiles of Fig. 5 are thus dominated by bands from CT_A and CT_B and it is still difficult to retrieve the contribution of spectral component **C**. Fig. 6 shows the experimental and simulated full 2D nutation spectra obtained of a Hahn echo detected nutation experiment. The simulated 2D spectrum includes CT_A and ST_A. From the simulated 2D spectrum it is clear that CT_A exhibits a broad range of nutation frequencies (similar to Fig. 5), but the dominant component is found just below $\sim 2 \times \nu_{RF}$. CT_B and eventual other components with large quadrupolar interactions will only contribute to the signal at $2 \times \nu_{RF}$. The satellites transitions, on the other hand, show their characteristic, discrete, frequency-dependent nutation frequencies. The limited excitation bandwidth of the probe reduces the observed span of the satellites. The characteristic butterfly-like pattern of the nutation frequencies of the ST is also found in the experimental 2D nutation spectrum, again with positive amplitudes for all frequencies. Considering the low intensity of these nutation profiles (compare also the relative intensities in the simulated spectrum), it is quite remarkable that these features show up so prominently. Besides the signal from CT_A and CT_B we do not observe the presence of nutation frequencies at $2 \times \nu_{RF}$, suggesting the absence of additional broadened CT's. The

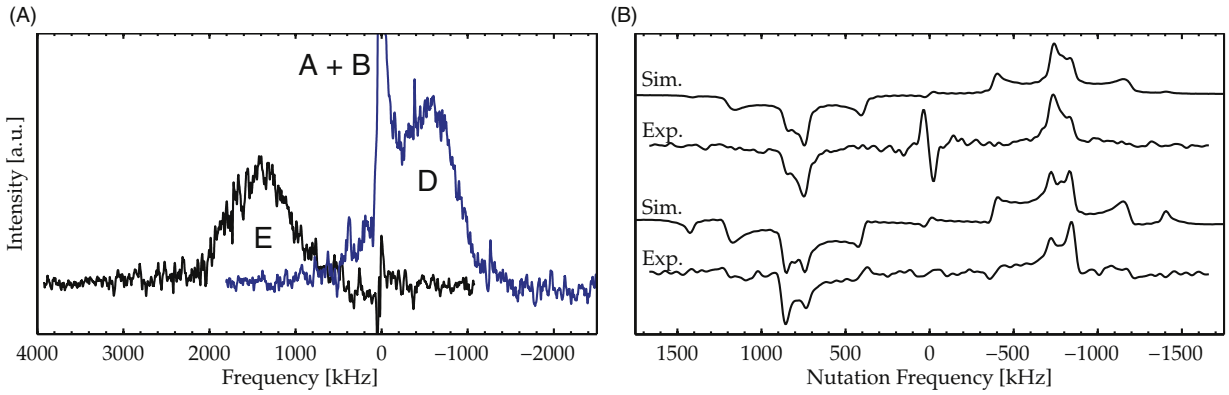

Fig. 7. (A) Off-resonance ^{35}Cl Hahn echo spectra of the $MgCl_2$ adduct; transmitter offset at 77.6 MHz (blue) and 79.7 MHz (black). It shows spectral components **D** and **E**. (B) Simulated and experimental ^{35}Cl nutation spectrum for the $MgCl_2$ adduct at ν_{RF} = 495 kHz at a frequency of 77.6 MHz (−700 kHz off-resonance). The simulations include the contribution from CT_A and ST_A. Top traces: The nutation experiments processed by Fourier transformation of the echo maxima. Bottom traces: Spectra taken as slices from the full 2D nutation spectrum at the position of the CT (78.3 MHz). (For interpretation of the references to colour in this figure legend, the reader is referred to the web version of this article.)

on-resonance nutation experiments strongly suggests that spectral component **C** can be assigned to be part of the ST of bulk $MgCl_2$ (ST_A).

3.4. Off-resonance nutation

The on-resonance experiments are dominated by spectral component **A**, the CT of the bulk Cl signal in $MgCl_2$, which partially obscures the signals from the satellites. The on-resonance nutation spectrum indicates that spectral component **C** is due to the ST of bulk $MgCl_2$. To verify that no contributions of other broadened components are present nutation spectra are taken at a large resonance offset so that contributions of the bulk CT is strongly diminished. Fig. 4 shows the ^{35}Cl Hahn echo spectra of the $MgCl_2$ adduct taken at a range of offsets. Fig. 7A shows the spectrum obtained at 77.6 MHz (−700 kHz off-resonance from the CT) in more detail. Comparable to Fig. 3, the spectrum contains the CT around 0 kHz and a ∼2 MHz featureless broad signal centred around the transmitter; we will refer to this as spectral component **D**. Although CT_A still dominates the spectrum on the vertical scale, component **D** is now relatively much more intense compared to component **C** in Fig. 3 as also becomes clear from the off-resonance nutation spectra. The contribution from spectral component **B** is also strongly diminished in the off-resonance spectra.

The top spectra in Fig. 7B show the nutation profile obtained from Fourier transformation of the echo maxima of the FID. The introduction of a resonance offset alters the mixture of the $|I, m\rangle$ states during the pulse which can again be described by evolution of the density matrix under the appropriate Hamiltonian [32]. The experimental trace shows two peaks at 740 and 840 kHz which are also observed in the simulation, that includes contributions from CT_A and ST_A. However, the other features in the simulation (400, 1150 and 1400 kHz) are barely observed in the experiment. As can be seen from the traces of the 2D nutation spectra at the position of the CT of bulk $MgCl_2$ (Fig. 7B, bottom spectra) those features all belong to components resulting from the off-resonance nutation [32] of CT_A, the CT of bulk $MgCl_2$. The signals at 400, 1150 and 1400 kHz are more prominent in both the simulated as well as the experimental trace. Also the changed relative intensities of the peaks around 800 kHz match well.

The simulated 2D nutation spectrum (see Fig. 8A) shows a banana-shaped feature in F1 at 700–800 kHz for the part of the satellite pattern that is close to the transmitter offset. This feature can be recognized in the experimental 2D spectrum as well. Similar to the on-resonance nutation spectrum, the central transition exhibits a broad range of nutation frequencies, although there are 2 dominant components at approximately 740 and 850 kHz as was clear from the 1D nutation spectrum. The satellite signal on the left (high frequency) side of the CT shows one nutation ridge. The further away from the central transition, the lower the apparent nutation frequency becomes. This part of the satellite pattern is not detected anymore under the experimental conditions due to limited bandwidth of the probe and hence the signal that is simulated for this, is not visible in the experimental 2D spectrum. The off-resonance nutation experiment shows good agreement between experiment and theory and thus clearly shows that spectral component **D** is part of the satellite transition of the bulk phase of the $MgCl_2$ nanoparticles. There are no indications of additional CT contributions of other distorted sites to the line shape.

When the transmitter is put at even larger offset from CT_A, the contribution from this CT will diminish even more. This can be seen in Fig. 7A which also shows the Hahn echo spectrum obtained at a transmitter frequency of 79.7 MHz (+1.4 MHz off-resonance). In the echo spectrum hardly any signal is left for the CT of bulk $MgCl_2$ while again there is a broad band of almost 2 MHz (spectral component **E**). The experimental nutation spectrum, see Figs. 9 and SI 6, will thus almost exclusively be composed of contributions from this component. Similar to the −700 kHz off-resonance nutation experiment, the ST display a banana-shaped pattern centred around the transmitter offset. As the CT lays outside the bandwidth of the probe, we do not observe the broad range of nutation frequencies at −1400 kHz in the experimental spectrum. We only observe a banana-shaped pattern which clearly originates from the ST. Even the asymmetry matches perfectly with the simulation, which shows that more intensity is observed on the right-hand side. This off-resonance nutation spectrum was acquired in only 19 h. There is excellent agreement between experimental and simulated nutation spectra. Again we find no evidence for the contribution of additional components. We therefore conclude that all the broad spectral components observed at different resonance offsets **C**, **D** and **E** are solely composed of one signal which is part of the satellite pattern of the $MgCl_2$ bulk phase (ST_A).

4. Conclusion

In this contribution we demonstrated the use of nutation NMR to characterize the ^{35}Cl spectrum of a model system for Ziegler-Natta catalysis: the binary adduct $MgCl_2$/DMDOMe. Owing to a millicoil allowing the generation of very high radiofrequency field

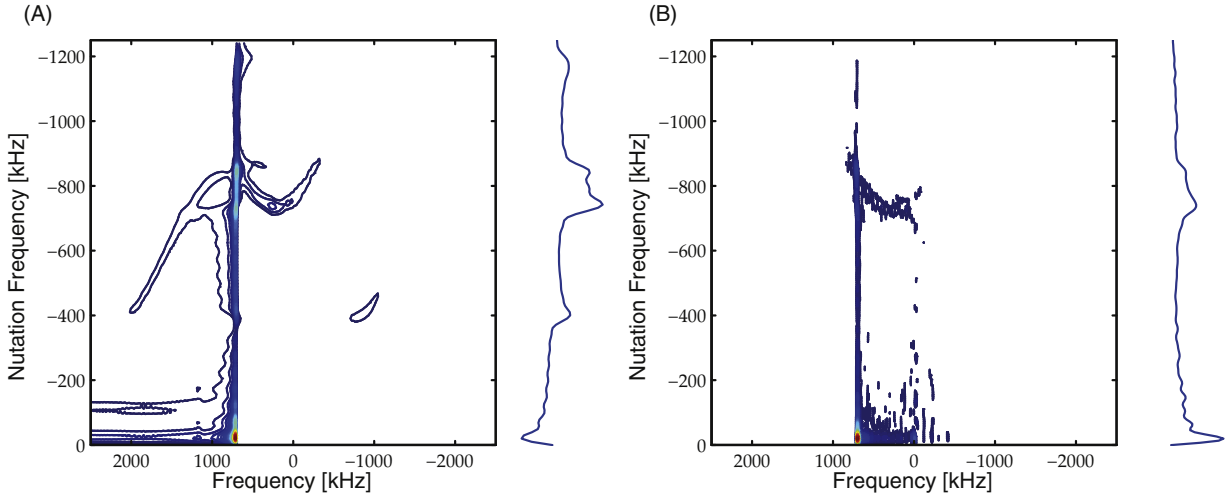

Fig. 8. (A) Simulated and (B) experimental off-resonance (−700 kHz) full 2D ^{35}Cl nutation spectra for the $MgCl_2$ adduct at an external magnetic field strength of 18.8 T and a ν_{RF} of 495 kHz. The experiment was measured accumulating 14,336 scans per echo, 80 increments and took 64 h to complete.

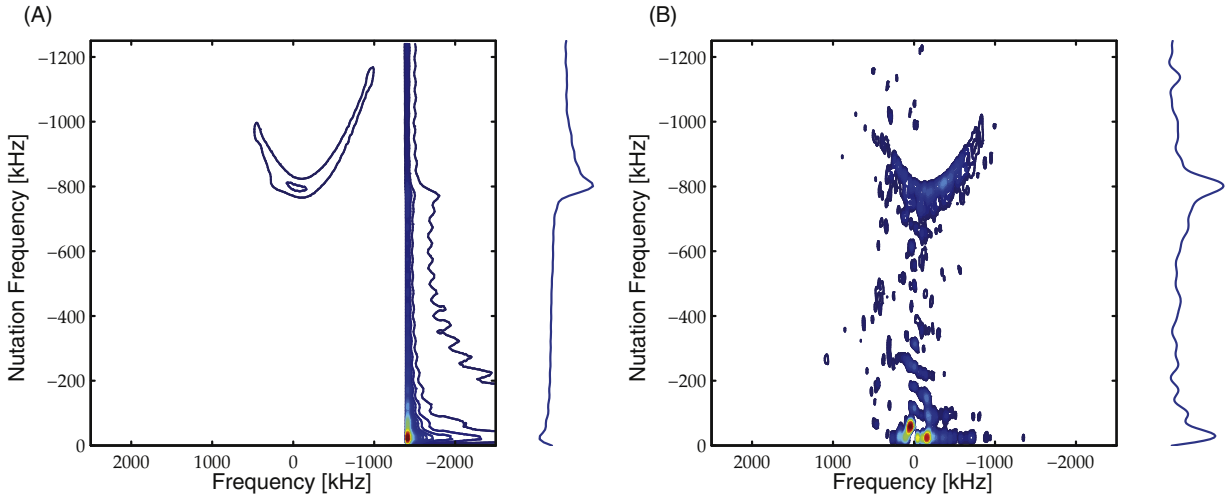

Fig. 9. (A) Simulated and (B) experimental off-resonance (+1400 kHz) full 2D ^{35}Cl nutation spectra for the $MgCl_2$ adduct at an external magnetic field strength of 18.8 T and a ν_{RF} of 480 kHz. The experiment was measured accumulating 2048 scans per echo, 40 increments and took 19 h to complete.

strengths we could detect a very broad spectrum showing multiple resonances. Spectral component **A** can be assigned to the bulk phase of $MgCl_2$ and component **B** to a surface site. A more detailed study of these surface sites in a series of binary adducts with different donors is underway. VOCS experiments suggested that components observed at different offsets (**C**, **D** and **E**) are part of the ST of bulk $MgCl_2$.

Nutation NMR was used to study the broad spectral features in detail. Simulations predict characteristic nutation profiles for satellite transitions, both under on-resonance as well as under off-resonance conditions, and show how it is possible to set the ST apart from broad CT's. Our experimental results match well with the simulations. We can therefore conclude that we observe broad spectral components that are part of satellite transitions. There are no signs of a distorted surface site other than component **B**.

Finally, it is worth noting that a full nutation experiment with decent S/N-ratio could be acquired within a day, while the full VOCS took more than a week of measurement time. With VOCS it is difficult to resolve overlapping CT and ST components of sites with different C_Q values and measurements at, at least, two different external field strengths are needed to confirm the nature of resonances. Nutation NMR thus proves to be a viable tool to analyze complex multicomponent systems where sites with largely different quadrupolar interaction parameters and a certain degree of disorder coincide.

5. Experimental

5.1. Sample preparation

Anhydrous $MgCl_2$ [9] and the organic donor DMDOMe were put together in a Retsch PM-100 planetary ball mill equipped with an airtight chemically inert ceramic jar (Y-stabilized ZrO_2). The jar (internal volume of 50 mL) was loaded inside a glovebox along with 87 g of grinding balls (also made of ZrO_2, diameter 3 mm). The sealed jar was then transferred into the mill. The rotation speed was set to the 650 rpm (maximum value), and the rotation motion was inverted at 20 min. intervals to prevent as far as possible encrustations on the inside walls of the jar. XRD measurements show that the $MgCl_2$ nanoparticles have average particle dimensions of $\langle L_c \rangle = 2.84$ and $\langle L_a \rangle = 4.37$ nm. Magnesium content of the sample has been quantified using ICP-OES. Solution state NMR of the adduct dissolved in deuterated methanol has been

used to quantify the donor content using an internal standard and was found to corresponds to 10% per Mg atom.

5.2. Solid-state NMR measurements

^{35}Cl spectra were recorded at room temperature on a Varian 800 MHz spectrometer (18.8 T, 78.3 MHz for ^{35}Cl) using a static home-built probe with an inner-coil diameter of 1.2 mm. Samples were packed in commercial 1.2 mm ZrO_2 rotors. Solid NaCl was used to calibrate the RF field strengths (ν_{RF} = 480 kHz) and as a chemical shift reference. The RF field strength at 77.6 MHz (ν_{RF} = 495 kHz) was calibrated after lowering the probe a few cm to the spot where the Cl resonance was found at 77.6 MHz. In the used settings the probe could tune from 74.1 MHz to 81.1 MHz. The RF field strength was assumed to be rather uniform over the whole frequency range also because the power output of the amplifier decreased by a maximum of 10% when going down in frequency to 74.1 MHz. ^{23}Na experiments were performed at room temperature on a Varian 400 MHz spectrometer (9.4 T, 105.8 MHz for ^{23}Na) using a commercial 3.2 mm probe.

To overcome problems related to probe ringing, all ^{35}Cl experiments (including the nutation experiments) are performed using a Hahn echo. Typical solid pulse lengths used are $\frac{\pi}{2}$ = 0.4 μs and π = 0.75 μs. To account for build-up of the pulse these pulse lengths are somewhat longer than expected from the RF field strength.

5.3. Simulations

The simulations of nutation spectra are performed using either Simpson [36] or an in-house MATLAB implementation of regular density matrix formalisms (available on request). Simulations for ^{23}Na are performed using a quadrupolar coupling parameter C_Q of 2.6 MHz with η = 0.58 for $NaSO_4$ and C_Q = 5.0 MHz with η = 0.2 for a fictive spin system. Simulations were run using 196,417 crystal orientations using the ZCW scheme [37]. For ^{35}Cl C_Q was set to either 4.6 MHz or 10 MHz for component **A** and **B**. Because of the distributed line shape of $MgCl_2$ η is set to 0.6 and 17,710 crystal orientations were run using the ZCW scheme. The simulations do not take into account the probe detection bandwidth and thus produces the full quadrupolar line shape. Hence, they will always include more signal from ST than the experiment. However, using the full 2D nutation experiment, it is possible to deduce the contributions from the different transitions by taking traces at appropriate positions.

Acknowledgement

This research forms part of the research programme of the Dutch Polymer Institute (DPI), project #793. Support of the Dutch Organization for scientific research NWO for the Solid state NMR facility for advanced materials science in Nijmegen is gratefully acknowledged. The authors acknowledge the technical support with the SSNMR measurements provided by Hans Janssen, Ruud Aspers and Gerrit Janssen. Dr. E. van Eck is acknowledged for useful comments on the manuscript and prof. V. Busico and G. Antinucci from the university of Naples are acknowledged for providing the $MgCl_2$ adduct.

Appendix A. Supplementary material

The supplementary information contains additional ^{35}Cl VOCS and simulated and experimental 1D and 2D nutation spectra. Supplementary data associated with this article can be found, in the online version, at http://dx.doi.org/10.1016/j.jmr.2017.06.002.

References

[1] A.S. Bazhenov, P. Denifl, T. Leinonen, A. Pakkanen, M. Linnolahti, T.A. Pakkanen, Modeling coadsorption of titanium tetrachloride and bidentate electron donors on magnesium dichloride support surfaces, J. Phys. Chem. C 118 (48) (2014) 27878–27883, http://dx.doi.org/10.1021/jp508693h.
[2] R. Credendino, D. Liguori, G. Morini, L. Cavallo, Investigating phthalate and 1,3-diether coverage and dynamics on the (104) and (110) surfaces of mgcl$_2$-supported Ziegler-Natta catalysts, J. Phys. Chem. C 118 (15) (2014) 8050–8058, http://dx.doi.org/10.1021/jp501390e.
[3] D. Partin, M. O'Keeffe, The structures and crystal chemistry of magnesium chloride and cadmium chloride, J. Solid State Chem. 95 (1) (1991) 176–183, http://dx.doi.org/10.1016/0022-4596(91)90387-w.
[4] M. Vittadello, P.E. Stallworth, F.M. Alamgir, S. Suarez, S. Abbrent, C.M. Drain, V. Di Noto, S.G. Greenbaum, Polymeric δ-$MgCl_2$ nanoribbons, Inorg. Chim. Acta 359 (8) (2006) 2513–2518, http://dx.doi.org/10.1016/j.ica.2006.01.044.
[5] P. Corradini, V. Barone, R. Fusco, G. Guerra, A possible model of catalytic sites for the stereospecific polymerization of α-olefins on 1st generation and supported Ziegler-Natta catalysts, Gazz. Chim. Ital. 113 (9–10) (1983) 601–607.
[6] V. Busico, M. Causa, R. Cipullo, R. Credendino, F. Cutillo, N. Friederichs, R. Lamanna, A. Segre, V. Van Axel Castelli, Periodic DFT and high-resolution magic-angle-spinning (hr-mas) ^{1}H NMR investigation of the active surfaces of $MgCl_2$-supported Ziegler-Natta catalysts. The $MgCl_2$ matrix, J. Phys. Chem. C 112 (4) (2008) 1081–1089, http://dx.doi.org/10.1021/jp076679b.
[7] R. Credendino, V. Busico, M. Causà, V. Barone, P.H.M. Budzelaar, C. Zicovich-Wilson, Periodic DFT modeling of bulk and surface properties of $MgCl_2$, Phys. Chem. Chem. Phys. 11 (30) (2009) 6525–6532, http://dx.doi.org/10.1039/b905676a.
[8] R. Credendino, D. Liguori, Z. Fan, G. Morini, L. Cavallo, Toward a unified model explaining heterogeneous Ziegler-Natta catalysis, ACS Catal. 5 (9) (2015) 5431–5435, http://dx.doi.org/10.1021/acscatal.5b01076.
[9] E.S.M. Blaakmeer, G. Antinucci, V. Busico, E.R.H. van Eck, A.P.M. Kentgens, Solid-state NMR investigations of $MgCl_2$ catalyst support, J. Phys. Chem. C 120 (11) (2016) 6063–6074, http://dx.doi.org/10.1021/acs.jpcc.5b12606.
[10] E. Kundla, A. Samoson, E. Lippmaa, High-resolution nmr of quadrupolar nuclei in rotating solids, Chem. Phys. Lett. 83 (2) (1981) 229–232, http://dx.doi.org/10.1016/0009-2614(81)85451-6.
[11] P.P. Man, Encyclopedia of Analytical Chemistry, Wiley-Blackwell, 2000.
[12] A. Medek, J.S. Harwood, L. Frydman, Multiple-quantum magic-angle spinning nmr: a new method for the study of quadrupolar nuclei in solids, J. Am. Chem. Soc. 117 (51) (1995) 12779–12787, http://dx.doi.org/10.1021/ja00156a015.
[13] L. Frydman, J.S. Harwood, Isotropic spectra of half-integer quadrupolar spins from bidimensional magic-angle spinning nmr, J. Am. Chem. Soc. 117 (19) (1995) 5367–5368, http://dx.doi.org/10.1021/ja00124a023.
[14] A. Samoson, E. Lippmaa, 2D nmr nutation spectroscopy in solids, J. Magn. Reson. 79 (2) (1988) 255–268, http://dx.doi.org/10.1016/0022-2364(88)90218-1.
[15] A.P.M. Kentgens, Quadrupolar nutation spectroscopy, in: Encyclopedia of Magnetic Resonance, John Wiley & Sons, Ltd, 2011, http://dx.doi.org/10.1002/9780470034590.emrstm0359.pub2.
[16] W. Franssen, Y. Rezus, A. Kentgens, High radio-frequency field strength nutation nmr of quadrupolar nuclei, J. Magn. Reson. 273 (2016) 33–39, http://dx.doi.org/10.1016/j.jmr.2016.09.018.
[17] R.W. Schurko, Ultra-wideline solid-state nmr spectroscopy, Acc. Chem. Res. 46 (9) (2013) 1985–1995, http://dx.doi.org/10.1021/ar400045t.
[18] R. Bhattacharyya, L. Frydman, Quadrupolar nuclear magnetic resonance spectroscopy in solids using frequency-swept echoing pulses, J. Chem. Phys. 127 (19) (2007) 194503, http://dx.doi.org/10.1063/1.2793783.
[19] L.A. O'Dell, The wurst kind of pulses in solid-state nmr, Solid State Nucl. Magn. Reson. 55-56 (2013) 2841, http://dx.doi.org/10.1016/j.ssnmr.2013.10.003.
[20] F.H. Larsen, H.J. Jakobsen, P.D. Ellis, N.C. Nielsen, Sensitivity-enhanced quadrupolar-echo nmr of half-integer quadrupolar nuclei. magnitudes and relative orientation of chemical shielding and quadrupolar coupling tensors, J. Phys. Chem. A 101 (1997) 8597–8606.
[21] F.H. Larsen, J. Skibsted, H.J. Jakobsen, N.C. Nielsen, Solid-state qcpmg nmr of low-γ quadrupolar metal nuclei in natural abundance, J. Am. Chem. Soc. 122 (29) (2000) 7080–7086, http://dx.doi.org/10.1021/ja0003526.
[22] L.A. O'Dell, R.W. Schurko, Qcpmg using adiabatic pulses for faster acquisition of ultra-wideline nmr spectra, Chem. Phys. Lett. 464 (1–3) (2008) 97–102, http://dx.doi.org/10.1016/j.cplett.2008.08.095.
[23] L.A. O'Dell, A.J. Rossini, R.W. Schurko, Acquisition of ultra-wideline nmr spectra from quadrupolar nuclei by frequency stepped wurst-qcpmg, Chem. Phys. Lett. 468 (4–6) (2009) 330–335, http://dx.doi.org/10.1016/j.cplett.2008.12.044.
[24] A.J. Rossini, R.W. Mills, G.A. Briscoe, E.L. Norton, S.J. Geier, I. Hung, S. Zheng, J. Autschbach, R.W. Schurko, Solid-state chlorine nmr of group iv transition metal organometallic complexes, J. Am. Chem. Soc. 131 (9) (2009) 3317–3330, http://dx.doi.org/10.1021/ja808390a.
[25] A.J. Rossini, I. Hung, S.A. Johnson, C. Slebodnick, M. Mensch, P.A. Deck, R.W. Schurko, Solid-state ^{91}Zr nmr spectroscopy studies of zirconocene olefin polymerization catalyst precursors, J. Am. Chem. Soc. 132 (51) (2010) 18301–18317, http://dx.doi.org/10.1021/ja107749b.
[26] K.E. Johnston, C.A. O'Keefe, R.M. Gauvin, J. Trbosc, L. Delevoye, J.-P. Amoureux, N. Popoff, M. Taoufik, K. Oudatchin, R.W. Schurko, A study of transition-metal

organometallic complexes combining ^{35}Cl solid-state nmr spectroscopy and ^{35}Cl nqr spectroscopy and first-principles DFT calculations, Chem. Eur. J. 19 (37) (2013) 12396–12414, http://dx.doi.org/10.1002/chem.201301268.

[27] C. Degen, M. Tomaselli, B.H. Meier, M.M.A.J. Voncken, A.P.M. Kentgens, Nmr investigation of atomic ordering in $Al_xGa_{1-x}As$ thin films, Phys. Rev. B 69 (19) (2004), http://dx.doi.org/10.1103/physrevb.69.193303, 193303-1.

[28] P.J. Knijn, P.J.M. van Bentum, E.R.H. van Eck, C. Fang, D.L.A.G. Grimminck, R.A. de Groot, R.W.A. Havenith, M. Marsman, W.L. Meerts, G.A. de Wijs, A solid-state NMR and DFT study of compositional modulations in $Al_xGa_{1-x}As$, Phys. Chem. Chem. Phys. 12 (37) (2010) 11517, http://dx.doi.org/10.1039/c003624b.

[29] F. Chen, Aluminum coordination and lewis acidity in transition aluminas, J. Catal. 133 (2) (1992) 263–278, http://dx.doi.org/10.1016/0021-9517(92)90239-e.

[30] H. Kraus, R. Prins, A.P.M. Kentgens, A ^{27}Al mqmas and off-resonance nutation nmr investigation of mo-p/γ-Al_2O_3 hydrotreating catalyst precursors, J. Phys. Chem. 100 (40) (1996) 16336–16345, http://dx.doi.org/10.1021/jp961574m.

[31] S. Kohn, M. Smith, P. Dirken, E. van Eck, A. Kentgens, R. Dupree, Sodium environments in dry and hydrous albite glasses: Improved ^{23}Na solid state nmr data and their implications for water dissolution mechanisms, Geochim. Cosmochim. Acta 62 (1) (1998) 79–87, http://dx.doi.org/10.1016/s0016-7037(97)00318-9.

[32] A. Kentgens, Off-resonance nutation nuclear magnetic resonance spectroscopy of half-integer quadrupolar nuclei, Prog. Nucl. Magn. Reson. Spectrosc. 32 (2) (1998) 141–164, http://dx.doi.org/10.1016/s0079-6565(98)00015-6.

[33] H. Koller, G. Engelhardt, A.P.M. Kentgens, J. Sauer, ^{23}Na nmr spectroscopy of solids: Interpretation of quadrupole interaction parameters and chemical shifts, J. Phys. Chem. 98 (6) (1994) 1544–1551, http://dx.doi.org/10.1021/j100057a004.

[34] S. Ashbrook, High-resolution nmr of quadrupolar nuclei in solids: the satellite-transition magic angle spinning (stmas) experiment, Prog. Nucl. Magn. Reson. Spectrosc. 45 (1–2) (2004) 53–108, http://dx.doi.org/10.1016/j.pnmrs.2004.04.002.

[35] I. Hung, R.W. Schurko, Solid-state ^{91}Zr nmr of bis(cyclopentadienyl) dichlorozirconium(iv), J. Phys. Chem. B 108 (26) (2004) 9060–9069, http://dx.doi.org/10.1021/jp040270u.

[36] M. Bak, J.T. Rasmussen, N.C. Nielsen, Simpson: a general simulation program for solid-state nmr spectroscopy, J. Magn. Reson. 147 (2) (2000) 296–330, http://dx.doi.org/10.1006/jmre.2000.2179.

[37] V.B. Cheng, H.H. Suzukawa, M. Wolfsberg, Investigations of a nonrandom numerical method for multidimensional integration, J. Chem. Phys. 59 (8) (1973) 3992–3999, http://dx.doi.org/10.1063/1.1680590.